analytical chemistry

Article

Cite This: Anal. Chem. 2018, 90, 13591−13599

pubs.acs.org/ac

Thermal Imaging as a Noncontact Inline Process Analytical Tool for Product Temperature Monitoring during Continuous Freeze-Drying of Unit Doses

Pieter-Jan Van Bockstal,[†] Jos Corver,[‡] Laurens De Meyer,[†] Chris Vervaet,[§] and Thomas De Beer*[,†]

[†]Laboratory of Pharmaceutical Process Analytical Technology (LPPAT), Department of Pharmaceutical Analysis, Faculty of Pharmaceutical Sciences, Ghent University, Ottergemsesteenweg 460, 9000 Ghent, Belgium

[‡]RheaVita, IIC UGent, Technologiepark Zwijnaarde-3, PO-box 17, 9052 Ghent, Belgium

[§]Laboratory of Pharmaceutical Technology, Department of Pharmaceutics, Faculty of Pharmaceutical Sciences, Ghent University, Ottergemsesteenweg 460, 9000 Ghent, Belgium

Supporting Information

ABSTRACT: Freeze-drying is a well-established technique to improve the stability of biopharmaceuticals which are unstable in aqueous solution. To obtain an elegant dried product appearance, the temperature at the moving sublimation interface T_i should be kept below the critical product temperature $T_{i,crit}$ during primary drying. The static temperature sensors applied in batch freeze-drying provide unreliable T_i data due to their invasive character. In addition, these sensors are incompatible with the continuous freeze-drying concept based on spinning of the vials during freezing, leading to a thin product layer spread over the entire inner vial wall. During continuous freeze-drying, the sublimation front moves from the inner side of the vial toward the glass wall, offering the unique opportunity to monitor T_i via noncontact inline thermal imaging. Via Fourier's law of thermal conduction, the temperature gradient over the vial wall and ice layer was quantified, which allowed the exact measurement of T_i during the entire primary drying step. On the basis of the obtained thermal images, the infrared (IR) energy transfer was computed via the Stefan−Boltzmann law and the dried product mass transfer resistance (R_p) profile was obtained. This procedure allows the determination of the optimal dynamic IR heater temperature profile for the continuous freeze-drying of any product. In addition, the end point of primary drying was detected via thermal imaging and confirmed by inline near-infrared (NIR) spectroscopy. Both applications show that thermal imaging is a suitable and promising process analytical tool for noninvasive temperature measurements during continuous freeze-drying, with the potential for inline process monitoring and control.

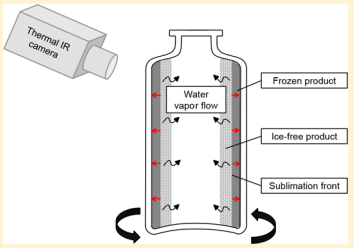

1. INTRODUCTION

Biopharmaceutical therapeutics are often formulated as dried products through freeze-drying (lyophilization) due to their limited stability in aqueous solution during distribution and storage.[1] For several decades, freeze-drying of (bio)-pharmaceutical unit doses has been operated in the traditional batchwise mode. All glass vials are filled with the aqueous drug formulation and loaded onto the shelves in the freeze-dryer. These vials make up one batch, which is processed through a sequence of consecutive process steps, i.e., freezing, primary drying, and secondary drying, until the final dried product is obtained.

Product appearance is an important critical quality attribute (CQA) of freeze-dried drug products. Loss of cake structure (i.e., cake collapse) should be avoided for aesthetic purposes and to ensure fast reconstitution of the dried product.[2] Therefore, the product temperature at the sublimation interface T_i should be kept below the critical product temperature $T_{i,crit}$ during the entire primary drying process. $T_{i,crit}$ is defined as the eutectic temperature T_e or the collapse temperature T_c for crystalline and amorphous products, respectively.[3] In general, T_c lies a few degrees above the glass transition temperature T_g' of the maximum freeze-concentrated drug formulation as the high viscosity of the glass near T_g' limits molecular motion.[3] Mechanistic models allow the determination of the optimal combination of the adaptable process parameters shelf temperature T_s and chamber pressure P_c to avoid exceeding $T_{i,crit}$ while maximizing the primary drying efficiency.[4−10] The development of this optimal dynamic profile of T_s and P_c requires the reliable measurement of T_i.

In batch freeze-drying, T_i is generally measured using resistance temperature detectors (RTDs) or thermocouples.[11] RTDs provide a mean readout for the entire area of the detection element, which is partially in contact with dried material during the majority of the primary drying process, leading to unreliable data. Thermocouples are preferred, as the temperature is only measured at the point where the two thin wires, made of different metals or metal alloys, are connected, making them less unreliable than RTDs in measuring T_i. The

Received: August 20, 2018
Accepted: October 19, 2018
Published: October 19, 2018

DOI: 10.1021/acs.analchem.8b03788
Anal. Chem. 2018, 90, 13591−13599

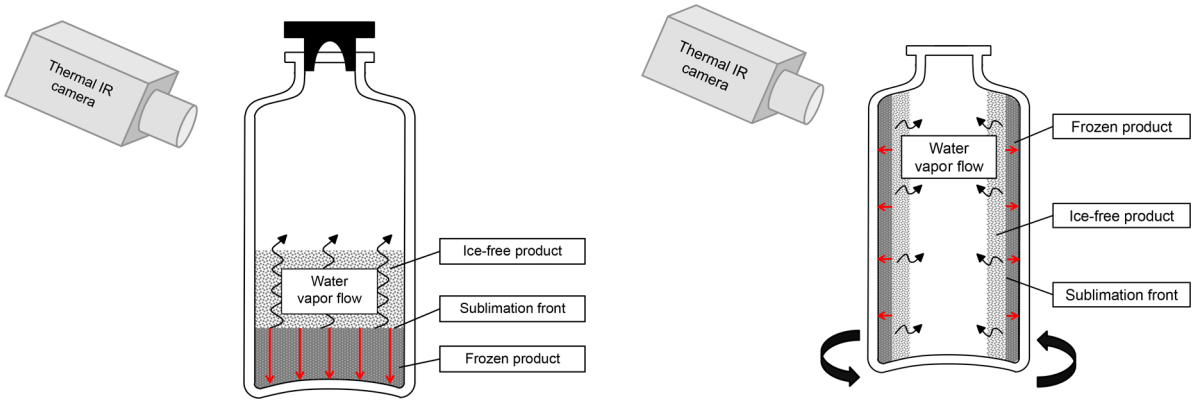

Figure 1. Illustration of the compatibility of thermal imaging with batch (left) and continuous (right) freeze-drying. The direction of the sublimation front during primary drying is indicated by the red arrows.

invasive character of both RTDs and thermocouples alters the process conditions for vials containing these sensors in comparison to vials in which they are absent. During the freezing step, the insertion of temperature sensors induces ice nucleation, i.e., a lower degree of supercooling, related to the formation of larger ice crystals.[12] In addition to faster drying kinetics due to the reduced product resistance in the monitored vials, the presence of these sensors adds to the heat transfer, contributing to the increased sublimation rate.[13] Therefore, the monitored vials containing a temperature sensor are not representative of the rest of the batch: i.e., atypical vials.[14−18] The response of the thermocouple is also highly dependent on its position in the ice because of the temperature gradient across the frozen product.[11] Deviations in its positioning in combination with the gradual downward movement of the sublimation front add to the high uncertainty in the measurement of the correct value of T_i.

In addition to unreliable temperature measurements, batch freeze-drying is inherently associated with several disadvantages, as previously described.[19,20] To resolve these disadvantages, a continuous freeze-drying concept for unit doses is proposed where each single process step is integrated in a continuous production flow.[21] This continuous concept is based upon the spinning of the vials during freezing, leading to a thin product layer spread over the entire inner vial wall. Primary and secondary drying operations are conducted in separate process units where individual IR heaters provide the noncontact radiative energy transfer to the spin-frozen vials. Opposite to the separation by time approach characteristic for batch freeze-drying, the consecutive process steps in the continuous concept are separated by space. As the continuous freeze-drying concept has already been extensively described, further details are provided in the Supporting Information.[19−21]

In a previous study, a mechanistic model was developed which allowed the computation of the optimal dynamic temperature profile of the IR heater to maximize the primary drying efficiency for each individual spin-frozen vial, while an elegant product appearance was maintained.[22] The development of the optimal IR heater profile for a specific formulation requires the reliable measurement of T_i. Thermocouples are not suitable to measure T_i during the continuous primary drying step. The spinning of the glass vials makes it impossible to insert thermocouples in the frozen product layer during the continuous freezing step. Estimating T_i by measuring the temperature of the outer glass wall is compromised by poor contact between the thermocouple and the glass due to rotation of the vial, leading to an overestimation of the temperature.

Thermal imaging allows noncontact temperature measurements on the basis of the detection of IR radiation emitted by an object and its conversion to a thermal image, displaying the spatial temperature distribution. Previously, this technique has been considered for inline temperature monitoring during batch freeze-drying.[23] The IR camera was implemented on the top of the freeze-dryer, which required customization of the equipment by removing a part of the radiation shield to visualize the vials on the top shelf. From the position where the IR camera was installed, only the top of the cake was visualized. As the sublimation front moves gradually downward during primary drying, most of the time the temperature of the dried product is measured, which is not representative of T_i. In addition, it is not possible to quantify the temperature gradient over the dried product layer. Monitoring the edge vials from the side is not an alternative option because of the extra radiant heat transfer from the chamber walls.[24] In addition to the fact that these edge vials are not representative of the rest of the batch, the radiant energy transfer through the vial walls results in a downward curved sublimation front which loses contact with the vial wall relatively shortly after the start of primary drying.[25] Consequently, thermal imaging is incompatible with batch freeze-drying for monitoring T_i during the entire primary drying process, as illustrated in Figure 1 (left). In the continuous freeze-drying concept, the vials are not packed on shelves but freely rotate in front of an individual IR heater, forming a long line of vials.[20] The product is spread over the entire wall of the spin-frozen vial, which allows complete visualization by the IR camera (Figure 1, right). The sublimation front moves from the center of the vial toward the glass wall during the continuous primary drying step. Hence, after compensation for the temperature gradient over the glass wall and the ice layer via Fourier's law of thermal conduction, T_i can be continuously monitored from the very beginning of the primary drying step until the end.

This study aims to demonstrate the feasibility of thermal imaging for real-time monitoring of the glass vial temperature during the primary drying stage of a continuous pharmaceutical freeze-drying process. The temperature gradient over the vial wall and ice layer is quantified via Fourier's law of thermal conduction for the accurate determination of T_i. As opposed to the invasive temperature sensors applied in the conventional batch process, this is the first demonstration of the

DOI: 10.1021/acs.analchem.8b03788
Anal. Chem. 2018, 90, 13591−13599

determination of the actual value for T_i for each unit dose during the entire primary drying stage in pharmaceutical freeze-drying. The use of thermal imaging will be evaluated for two different applications: the determination of the primary drying end point and the calculation of the dried product mass transfer resistance R_p.

2. MATERIALS AND METHODS

2.1. Experimental Freeze-Drying Setup. A 10 mL type I glass vial (Schott, Müllheim, Germany) was filled with 3.9 mL of an aqueous 3 mg/mL sucrose (Sigma-Aldrich, Saint Louis, MO, USA) solution and spin-frozen as previously described.[20] The glass vial was positioned in a vial holder and vertically rotated along its longitudinal axis at approximately 2900 rotations per minute (rpm). The solution was spread uniformly across the entire vial wall, after which the rotating vial was immersed into liquid nitrogen for 40 ± 5 s, leading to complete solidification of the product. Within 15 ± 5 s after spin-freezing, the vial was transferred from the liquid nitrogen to the drying chamber of an Amsco FINN-AQUA GT4 freeze-dryer (GEA, Köln, Germany), to avoid exceeding T_g' of the formulation. The vacuum chamber of this pilot-scale batch freeze-dryer was used as a model for the primary drying module of the continuous freeze-drying system. The shelves in the drying chamber were precooled at a temperature of −10 °C, which was maintained during the entire process to minimize its radiation contribution to the spin-frozen vial during drying. The vial was hung in front of one IR heater (Weiss Technik, Zellik, Belgium) at a distance of 40 mm measured from the center of the vial until the heated filaments of the IR heater, without making contact with the shelf (Figure 2). To achieve a homogeneous radiation energy transfer, the spin-frozen vial was continuously rotating at 5 rpm. After the vial was placed in the drying chamber, the pressure was immediately lowered to 13.3 Pa. Within 5 min, the pressure was below the triple point of water. After a total of 17 min, the desired pressure was reached and the IR heater was activated. Primary drying was conducted at a constant electric power input P_e of 7 W, supplied by the Voltcraft PPS-11360 power supply (Conrad Electronic, Hirschau, Germany) to the IR heater. The amount of ice sublimed during the initial pressure decrease, i.e., the 17 min period between activation of the vacuum pump and the IR heaters, was gravimetrically determined in triplicate.[22]

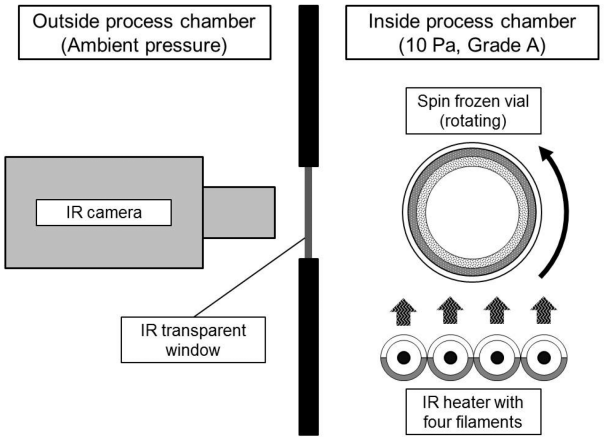

Figure 2. Illustration of the IR camera setup (top view) during primary drying with the rotating spin-frozen vial and the IR heater inside the vacuum chamber and the IR camera positioned outside with measurement through an IR-transparent window at an angle of 90°.

2.2. Thermal Imaging. The temperature of the spin-frozen vials was continuously monitored using a FLIR A655sc IR camera (Thermal Focus, Ravels, Belgium) equipped with a 45° lens and an uncooled microbolometer as detector. The thermal IR camera was placed outside the vacuum chamber, in front of the IR-transparent germanium window, through which the temperature of the vials was measured (Figure 2). The model-based approach as a rationale for germanium being a transparent material for the electromagnetic radiation emitted by the glass vials is described in the Supporting Information. The spin-frozen vial was slowly rotating (5 rpm) at a distance of 350 ± 10 mm from the camera. The depths of field far and near limit were approximately 380 and 320 mm, respectively. Hence, each object situated between these limits was in focus. The IR heater providing the energy for ice sublimation was positioned at an angle of 90° to the thermal camera (Figure 2). Thermal images were recorded with an image size of 640 × 480 IR pixels. Pixels from the surrounding IR window interface which did not contain any relevant information were removed from the thermal images. At the specified measuring distance, the width of the vial (24 mm) took up approximately 80 pixels, leading to a spatial resolution of 0.30 mm. The thermal resolution and spectral range of the IR camera are 30 mK noise equivalent temperature difference (NETD) and 7.5−14 μm, respectively. Each minute a thermal image was recorded via the FLIR ResearchIR MAX software (Thermal Focus, Ravels, Belgium). Data processing was conducted using the same software. The emissivity of the glass vial was 0.93. The temperature and humidity in the room outside the vacuum chamber were determined at the start and the end of the process.

2.3. Experimental Determination of Transmittance of Germanium IR Window. The spectral transmittance of the germanium IR window as a function of the vial temperature $T_B(T)$ was experimentally verified by comparing thermal images with thermocouple data. A glass vial completely filled with water was frozen using liquid nitrogen (without spinning) and hung in the drying chamber after freezing. Before freezing, a thermocouple was inserted in the glass vial; hence, it was completely immersed in ice. On the basis of the principle that ice temperature is related to its vapor pressure, the temperature of the ice was varied over the range of interest to monitor the temperature during primary drying. The pressure in the drying chamber was initially decreased until 10 Pa, which allowed measurement of the temperature starting from a lower limit of approximately −40 °C. The pressure in the drying chamber was increased in discrete steps of 0.25−0.50 Pa until 70 Pa, which was associated with a gradual increase in temperature until approximately −24 °C. At each pressure level, after sufficient equilibration, the temperature of the vial $T_{v,o}$ was measured with the thermal IR camera, positioned in front of the IR window. These measurements were correlated with the thermocouple output, allowing estimation of the transmittance of the germanium window as a function of the temperature of the glass vial. As will be discussed in further sections, for this experiment, the temperature gradient over the glass wall and the ice layer was assumed to be negligible, due to the very limited energy input to the vial, as no additional except for the radiation contribution of the surroundings was provided.

DOI: 10.1021/acs.analchem.8b03788
Anal. Chem. 2018, 90, 13591−13599

2.4. Calculation of Temperature Gradient over Glass Wall and Ice Layer. The IR camera measures the temperature of the outer side of the vial wall, although the temperature at the sublimation front during primary drying is critical and is thus of interest. Hence, the accurate measurement of the temperature at the sublimation interface T_i requires an appropriate compensation for the temperature gradient over the glass wall and the ice layer, which are in close contact with each other (Figure 3). Due to the endothermic

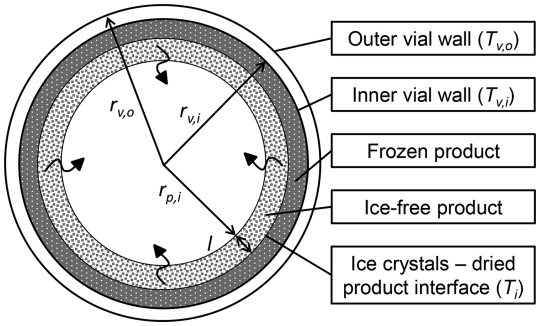

Figure 3. Illustration of a cross section of a spin-frozen vial during primary drying with specified temperatures and radii.

nature of the sublimation process, the radiation energy provided by the IR heaters during primary drying is completely consumed for ice sublimation and T_i remains constant. Therefore, the system can be assumed to be at steady state. Hence, the temperature gradient can be quantified by Fourier's law of thermal conduction, which states that the rate of heat flow per unit area is proportional to the temperature gradient.[26] After integration from the outer radius of the glass vial $r_{v,o}$ to the inner radius $r_{v,i}$ for the specific cylindrical geometry (Figure 3), the one-dimensional heat conduction over the glass wall of the vial is given by[26]

$$P_{tot} = 2\pi k_{glass} h \frac{T_{v,o} - T_{v,i}}{\ln\left(\frac{r_{v,i}}{r_{v,o}}\right)} \quad (1)$$

with P_{tot} being the total power provided to the spin-frozen vial (W), k_{glass} the thermal conductivity of glass (1.05 W/(m K)), h the height of the spin-frozen product (m), $T_{v,o}$ the temperature measured at the outer side of the vial wall (K), $T_{v,i}$ the temperature at the inner side of the vial wall (K), $r_{v,i}$ the inner radius of the glass vial (m), and $r_{v,o}$ the outer radius of the glass vial (m). The temperature gradient over the thin ice layer is also calculated via eq 1, in which $T_{v,o}$ and $T_{v,i}$ are replaced by $T_{v,i}$ and T_i (K) and $r_{v,o}$ and $r_{v,i}$ by $r_{v,i}$ and the sum of the radius from the center of the vial to the border of the spin-frozen layer $r_{p,i}$ (m) and the thickness of the dried product layer l (m), respectively (Figure 3). In addition, the thermal conductivity of ice. k_{ice} (2.18 W/(m K)), is taken into account instead of k_{glass}. Due to the close contact between the ice layer and the vial wall, the thermal contact resistance between the glass and ice can be ignored.[11]

The power provided by the IR heater to the spin-frozen vial during primary drying P_{rad} was calculated via the Stefan–Boltzmann law:[26]

$$P_{rad} = A_{rad} F \sigma (\varepsilon T_{rad}^4 - a T_{v,o}^4) \quad (2)$$

with A_{rad} being the surface area of the IR heater (m^2), F the view factor (−), σ the Stefan–Boltzmann constant (5.67×10^{-8} W/(m^2 K^4)), ε the emission coefficient of the IR heater (−), T_{rad} the temperature of the IR heater (K), and a the absorptivity of the glass vial (−). In general, a is estimated as the value of ε for a given surface, in this case the glass vial.[26] F is defined as the percentage of total radiation which leaves the surface of the IR heater and goes directly to the target surface: i.e., the spin-frozen vial.[27] F is computed on the basis of a Monte Carlo method previously described.[28] Finally, the radiation energy provided by the surrounding surfaces (e.g., the chamber walls and door) to the spin-frozen vial P_{sur} was experimentally determined as described in previous work.[22] Hence, P_{tot} was compensated for this additional energy contribution following eq 3:

$$P_{tot} = P_{rad} + P_{sur} \quad (3)$$

2.5. Determination of Dried Product Mass Transfer Resistance. During primary drying, the sublimation front gradually moves from the center of the vial toward the glass wall, leaving a porous product matrix (Figure 3). The water vapor generated at this sublimation interface escapes through this porous structure before reaching the condenser. The flow of water vapor through the pores is restricted by the dried product mass transfer resistance R_p. Exceeding this mass flow limit is associated with a local increase in vapor pressure at the sublimation interface $P_{w,i}$ due to the saturation of the pores. As T_i is in equilibrium with $P_{w,i}$, T_i will then also increase. However, T_i should be maintained below $T_{i,crit}$ during the entire primary drying step to avoid collapse of the product. Therefore, the accurate determination of R_p is essential for the development of the optimal freeze-drying cycle (i.e., the optimal dynamic IR heater temperature profile) for a specific formulation, allowing a maximum primary drying efficiency while yielding a decent cake aspect.[22]

The dried product mass transfer resistance R_p (m/s) is correlated to the ratio of the vapor pressure gradient between the sublimation interface and the drying chamber and the mass flow rate by the equation

$$R_p = \frac{A_p (P_{w,i} - P_{w,c})}{\dot{m}_{sub}} \quad (4)$$

with A_p being the product surface area available for sublimation (m^2), $P_{w,i}$ the vapor pressure of ice at the sublimation interface (Pa), $P_{w,c}$ the partial pressure of water in the drying unit (Pa), and $\dot{m}_{sub}$ the sublimation rate during primary drying (kg/s). $P_{w,c}$ is considered to be equal to the overall pressure in the drying unit P_c, as the gas composition in the primary drying unit consists almost entirely of water vapor, similar to batch freeze-drying.[6] The system was assumed to be at steady state (section 2.4); hence, $\dot{m}_{sub}$ is directly linked to P_{tot}. This relation is given by

$$\dot{m}_{sub} = \frac{P_{tot} M}{\Delta H_s} \quad (5)$$

where M is the molecular weight of water (0.018 kg/mol) and ΔH_s is the latent heat of ice sublimation (51139 J/mol). P_{tot} is determined via the Stefan–Boltzmann law, on the basis of the measurement of $T_{v,o}$ using the IR camera, including the compensation for P_{sur} (section 2.4). Alternatively, $\dot{m}_{sub}$ can also be determined via a gravimetric procedure, requiring a series of experiments. $P_{w,i}$ is in equilibrium with T_i, calculated by the empirical equation[29]

DOI: 10.1021/acs.analchem.8b03788
Anal. Chem. 2018, 90, 13591−13599

$$P_{w,i} = 3.6 \times 10^{12}\, e^{-6145/T_i} \quad (6)$$

where T_i is determined on the basis of the measured value of $T_{v,o}$, taking the temperature gradient over the glass wall and the ice layer into account (aection 2.4). The A_p value of the spin frozen layer is calculated by

$$A_p = 2\pi(r_{p,i} + l)h \quad (7)$$

where $r_{p,i}$ is given by

$$r_{p,i} = \sqrt{r_{v,i}^2 - \frac{V}{\pi h}} \quad (8)$$

with V being the filling volume (m^3). Due to the cylindrical shape of the cake, A_p increases with the gradual movement of the sublimation interface from the inside of the vial toward the vial wall (Figure 3).

R_p is formulation specific and is strongly influenced by the size of the pores in the dried product layer, which is mainly determined by the freezing procedure and the degree of supercooling during this freezing step.[30,31] In addition, as the path of water vapor originating from the sublimation front and flowing through the pores of the dried product layer is prolonged with the primary drying progress, R_p generally increases with the corresponding increase in l. This relation is given by the empirical equation[32]

$$R_p = R_{p,0} + \frac{A_{R_p} l}{1 + B_{R_p} l} \quad (9)$$

where $R_{p,0}$ (m/s), A_{R_p} (1/s) and B_{R_p} (1/m) are constants describing R_p in function of the thickness of the dried product layer l. R_p is calculated as a function of drying time t for a specified time interval Δt (e.g., 60 s) via eq 4. The increase in the dried layer thickness Δl (m) is calculated for the same Δt value by

$$\Delta l = \frac{\dot{m}_{sub} \Delta t}{A_p \rho_{ice} \phi} \quad (10)$$

with ρ_{ice} being the density of ice (kg/m^3) and ϕ the volume fraction of ice (−). Equation 9 is fitted to the experimental R_p data in function of l via nonlinear regression, resulting in the R_p constants.

2.6. NIR Spectroscopy. Diffuse reflectance NIR spectra were continuously collected inline with an Antaris II Fourier transform NIR spectrometer (Thermo Fisher Scientific, Erembodegem, Belgium), equipped with a quartz halogen lamp, a Michelson interferometer, and an InGaAs detector.[20] The fiber optic probe was implemented in the drying chamber at a distance of 0.5 ± 0.1 mm near the middle of the vial without hampering or disturbing the rotation of the vial. As drying progresses from the center of the vial to the inner vial wall, inline NIR spectroscopy allowed the detection of complete ice removal: i.e., the end point of primary drying. Every 20 s a NIR spectrum was collected in the 4500−10000 cm^{-1} region with a resolution of 16 cm^{-1} and averaged over four scans. The illumination spot size obtained with the NIR probe was approximately 28 mm^2. Due to rotation of the vial during the measurements, each spectrum was collected at a different position of the cake on a specific height. It was assumed that this monitored part is representative of the whole cake.

2.7. Multivariate Data Analysis. The collected NIR spectra during each validation run were analyzed with the help of the multivariate data analysis software SIMCA (Version 14.0.0, Umetrics, Umeå, Sweden).[20] The NIR spectra collected before activation of the heaters were removed from each data set. A Savitzky−Golay filter was applied to smooth the spectra: a quadratic polynomial function was fitted to a moving submodel, each containing 15 data points. Additionally, standard normal variate (SNV) preprocessing was applied to eliminate the additive baseline offset variations and multiplicative scaling effects in the spectra which may be caused by small variations in distance between the NIR probe and the rotating glass vial and possible differences in product density.[33] Principal component analysis (PCA) was then used for an analysis of the preprocessed and mean-centered NIR spectra.

PCA is an unsupervised multivariate projection method which extracts and displays the variation in the data set.[34,35] The original variables, e.g., the individual wave numbers of the NIR spectra, are replaced by a new set of latent variables, named principal components (PCs). These PCs are sequentially acquired by an orthogonal, bilinear decomposition of the data matrix. Each component explains most of the remaining variability in the data. PCs are composed of a score and a loading vector. The score vector contains a score value for each spectrum, which describes its quantitative relation to the other spectra. The loading vector provides qualitative information about which spectral features present in the original observations are captured by the corresponding component.

2.8. Determination of the Glass Transition Temperature. The T_g' value of the 3 mg/mL sucrose formulation was determined via modulated differential scanning calorimetry (MDSC) using a Q2000 differential scanning calorimeter (TA Instruments, New Castle, DE, USA). Hermetically sealed aluminum pans (TA Instruments, New Castle, DE, USA) were filled with approximately 12 mg of the formulation. The DSC cell was constantly purged with dry nitrogen at a flow rate of 50 mL/min. The sample was initially cooled until −90 °C. This temperature was maintained for 5 min. Subsequently the temperature was linearly increased until 0 °C at a heating rate of 2 °C/min. The modulation amplitude and period were set at 0.212 °C and 40 s, respectively. The analysis was conducted in duplicate. The thermal images were analyzed with TA Instruments Universal Analysis 2000 version 4.7A (TA Instruments, New Castle, DE, USA).

3. RESULTS AND DISCUSSION

3.1. Transmittance of Germanium IR Window. The experimentally verified spectral transmittance T_B through the germanium IR window is plotted as a function of the vial temperature $T_{v,o}$ in Figure 4. The transmittance T_B increases with $T_{v,o}$. The spectral radiance profile $B_\lambda(\lambda)$ emitted by the glass vials changes with $T_{v,o}$ (Figure S-1, Supporting Information). In turn, the transmittance of IR radiation by the germanium window depends on the wavelength of the radiation. The top of the IR radiation spectrum shifts to a lower wavelength for a higher temperature of the glass vials, while the transmission of germanium is higher at a lower wavelength (Figure S-2, Supporting Information). Hence, the transmittance of the IR radiation spectrum emitted by the glass vial is higher for a higher temperature of this vial.

A quadratic model was fitted to the experimental T_B data as a function of $T_{v,o}$. A t test indicated that the quadratic term is significant at the 5% significance level. The root mean square

DOI: 10.1021/acs.analchem.8b03788
Anal. Chem. 2018, 90, 13591−13599

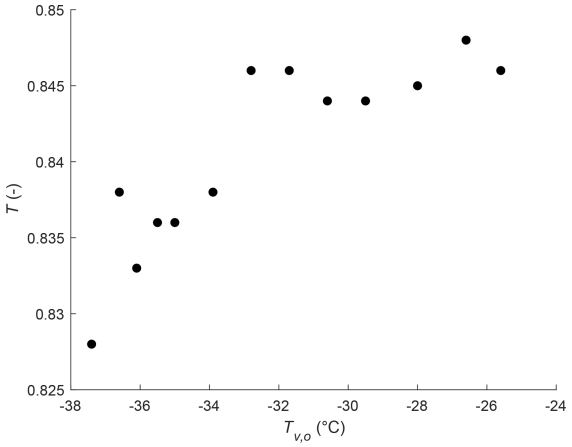

Figure 4. Spectral transmittance T_B of the germanium IR window as a function of the vial temperature $T_{v,o}$.

error of cross-validation (RMSECV) for the quadratic model was 0.002951. On the basis of these findings, the relation between T_B and $T_{v,o}$ for the temperature range under study was described by the (empirical) quadratic equation

$$T_B = -0.0001734T_{v,o}^2 + 0.08508T_{v,o} - 9.593 \quad (11)$$

with $T_{v,o}$ expressed in K.

3.2. Analysis of Thermal Images. The thermal images obtained at different time points during the primary drying of a spin-frozen vial are plotted in Figure 5. The left thermal image in Figure 5 shows a spin-frozen vial under constant vacuum (13.3 Pa), just before activation of the IR heater. Generally, the measured temperature $T_{v,o}$ was approximately −37 °C. In the middle (black arrow in left thermal image in Figure 5) and at the edge of the vial (red arrows in left thermal image in Figure 5), thin bands are present with temperature values deviating from the rest of the glass surface. These bands remained in the same position despite the rotation of the spin-frozen vial, indicating that they originated from external factors instead of being a characteristic of the monitored vial itself. Both bands originated from reflectance inherent to the experimental setup and resulted in a higher value for $T_{v,o}$. These observations were present in each thermal image recorded during the entire drying process. The deviating temperature data in these points do not represent a correct measurement of T_i; hence, these regions were excluded from further analysis.

The thermal image in the middle of Figure 5 was captured 20 min after activating the IR heater. $T_{v,o}$ had increased to approximately −33 °C, as the increased energy input led to a higher sublimation rate, associated with a local increase in $P_{w,i}$ and, naturally, T_i (section 2.5). The emitted radiation energy reflected on the vial side facing the IR heater (red arrow in middle thermal image in Figure 5), leading to unreliable $T_{v,o}$ data in that position. In combination with the previous findings, the region of interest for the correct and reliable measurement of $T_{v,o}$ was situated on the vial side facing away from the IR heater, as indicated by the black rectangle.

The third thermal image (Figure 5) was obtained after 100 min of primary drying. A steep increase in $T_{v,o}$ toward approximately −20 °C at the top part of the vial indicated ice removal was complete, as the provided radiation energy is no longer consumed for ice sublimation. Instead, the energy is used to heat up the glass vial and its content, associated with higher values for $T_{v,o}$. As $T_{v,o}$ at the middle and bottom of the vial remained approximately −32.5 °C, the thermal image indicates that primary drying was finished earlier in the top part of the spin-frozen layer in comparison to the bottom part. This observation can be explained by the difference in product layer thickness between the top and the bottom of the cake, originating from the spin-freezing step. Fast rotation of the vial results in a thin layer with a parabolic shape of the liquid surface. The inherent deviation in layer thickness between the top and the bottom of the vial is calculated by

$$\Delta L_{tot} = \frac{hg}{\omega^2 r_{p,i}} \quad (12)$$

with ΔL_{tot} being the deviation to the average thickness of the spin-frozen layer (m), g the gravitational acceleration (9.81 m/s^2), and ω the angular velocity (rad/s). For the maximum rotation speed of the current experimental setup (2900 rpm), the relative deviation in layer thickness between the cake at the top and the bottom of the vial is 29.7%. When the rotation speed is increased to 7000 rpm, which will be possible in future continuous freeze-drying manufacturing equipment, this relative deviation can be minimized until 5.00%, intended as the maximum allowable deviation in layer thickness between the top and bottom. The rotation speed can be adapted in the continuous freeze-drying prototype to ensure this condition is met, without being harmful for biopharmaceuticals.[36]

3.3. Temperature Monitoring. The temperature of the glass vial $T_{v,o}$ is plotted as a function of (primary) drying time t in Figure 6. In the left part of Figure 6, the temperature trajectory is plotted for each individual pixel from the rectangle indicated in black in the right thermal image from Figure 5. $T_{v,o}$ is equal for the complete vial during most of the primary drying step, while toward the end, $T_{v,o}$ starts to increase at different timings depending on the location on the vial. The

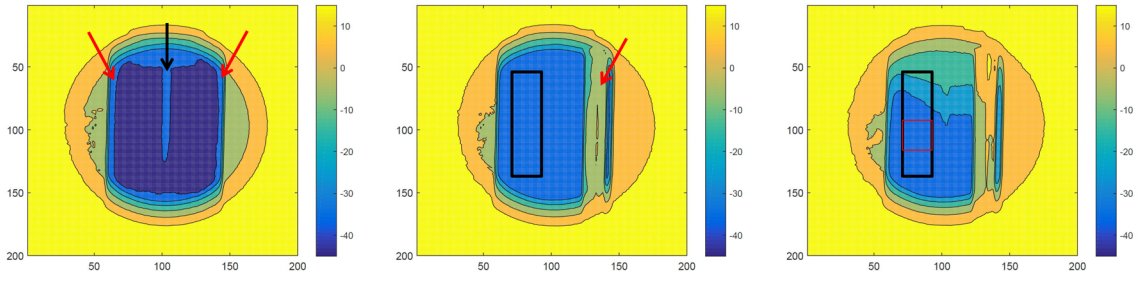

Figure 5. Thermal images of a spin-frozen vial just before activation of the IR heaters (left), after 20 min (middle), and after 100 min of primary drying (right). The arrows indicate regions on the vial wall which suffer from external reflectance, while the red and black rectangles indicate the region of interest for temperature monitoring.

DOI: 10.1021/acs.analchem.8b03788
Anal. Chem. 2018, 90, 13591−13599

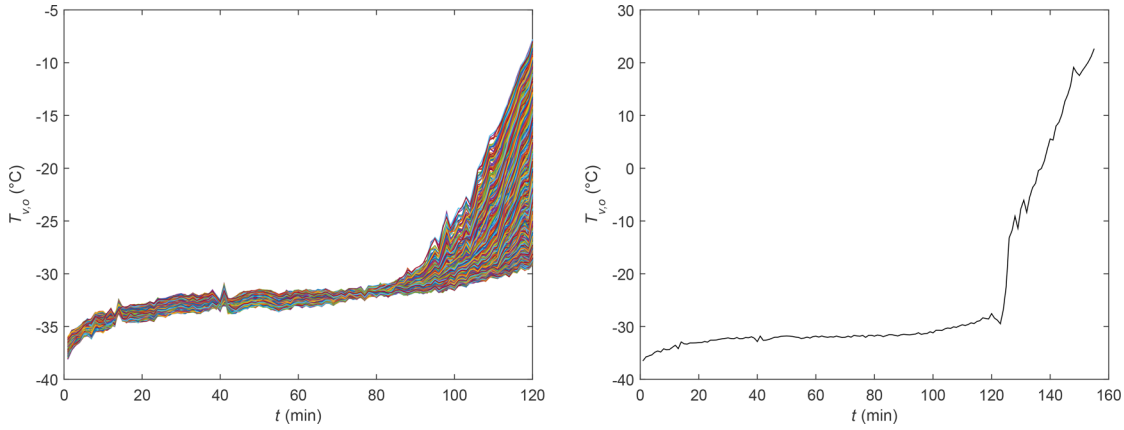

Figure 6. Temperature at the outer vial wall $T_{v,o}$ as a function of drying time t: (left) temperature profiles for each individual pixel within the black rectangle drawn on the vial shown in the right image of Figure 5; (right) mean value for $T_{v,o}$ calculated from the red rectangle drawn on the vial shown in the right image of Figure 5.

analysis of the thermal images indicated primary drying was finished earlier at the top of the cake compared to the bottom, which was attributed to the deviation in layer thickness between the top and bottom (section 3.2). For further calculations, the mean value of $T_{v,o}$ was calculated for the square region indicated in red in the right thermal image from Figure 5. This region was located in the middle of the vial, where the layer thickness approaches the average theoretical value of the spin-frozen product layer.

Initially, $T_{v,o}$ increases a few degrees until a plateau value is reached after approximately 25 min. This gradual temperature increase is caused by the increase in R_p, as will be discussed in section 3.5. Only after approximately 100 min does $T_{v,o}$ again start to increase, followed by a steep increase after 124 min. As observed in the right thermal image in Figure 5, a steep increase in $T_{v,o}$ indicates that the amount of ice is diminishing, as the provided energy is no longer consumed for sublimation but heats up the glass vial. As a confirmation, the primary drying end point was determined via the NIR spectroscopy method, which is extensively described in the literature.[20,22] This method is based on PCA to analyze the NIR spectra which were collected inline during the drying stage. This way, the primary drying end point was estimated to be reached after 128 min (data not shown). This value is in accordance with the data obtained by the IR camera and confirms the applicability of thermal imaging to determine the primary drying end point.

Via NIR spectroscopy, the primary drying progress is monitored at one specific height of the rotating vial while thermal imaging provides a two-dimensional image with additional spatial information. Hence, thermal imaging allows the monitoring of the drying behavior for the complete spin-frozen layer. Even multiple vials of the continuous belt could be monitored at once, offering a huge advantage to NIR spectroscopy, making use of a single probe at a fixed position in the drying chamber. Multipoint NIR spectroscopy could offer an alternative for the monitoring of multiple vials, while NIR chemical imaging could be applied to image the complete vial.[37,38] However, it is practically not possible to implement NIR chemical imaging for inline measurements. NIR spectroscopy and thermal imaging are highly complementary, as the former can provide detailed inline information about several CQAs such as residual moisture content, protein conformation, and the solid state of different components (e.g., mannitol), while the latter is an essential tool regarding product appearance by monitoring T_i (section 3.4).[37−41] Eventually, the combination of both thermal imaging and NIR spectroscopy will be implemented in the continuous freeze-drying equipment for optimal real-time process monitoring and control.

3.4. Temperature Gradient over Glass Wall and Ice Layer. The temperature at the sublimation front T_i is calculated on the basis of the measured temperature at the outer vial wall $T_{v,o}$ via Fourier's law of thermal conduction (section 2.4). $T_{v,o}$ and T_i are plotted as a function of t in Figure 7. During primary drying, the lowest temperature is situated at

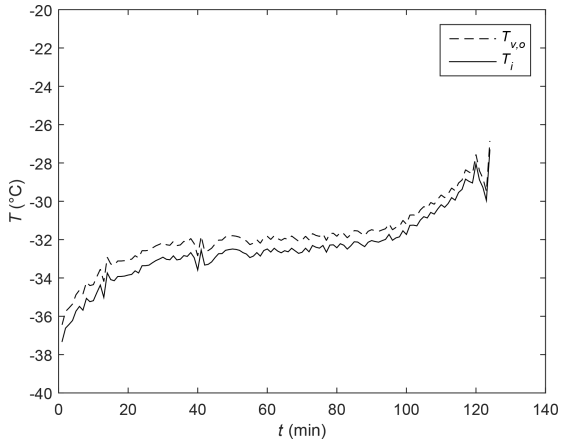

Figure 7. Temperature at the outer vial wall $T_{v,o}$ (dashed) and the temperature at the sublimation front T_i (solid) as a function of drying time t.

the sublimation interface. Hence, T_i is constantly lower than $T_{v,o}$ and energy is transferred from the outer glass wall toward the sublimation front. With the progress of primary drying, the ice layer thickness gradually decreases. Provided that the energy flux remains constant, the absolute temperature difference between $T_{v,o}$ and T_i also decreases (Figure 7). At the start of the primary drying step, the temperature gradient over the glass wall and ice layer was 0.88 °C. With the gradual decrease in ice layer thickness, the temperature gradient over the glass wall at the end of primary drying was 0.47 °C.

After approximately 100 min of primary drying, $T_{v,o}$ increases by a few degrees (Figure 7), despite the fact that

DOI: 10.1021/acs.analchem.8b03788
Anal. Chem. 2018, 90, 13591−13599

primary drying is only finished after 124 min (Figure 6). The NIR data indicate that traces of ice are still present at the time this small increase in temperature occurs (NIR data not shown). Possibly, the remaining low amount of ice might not sufficiently cool the glass vial, which might cause the gradual increase in $T_{v,o}$. Hence, from this moment on, the assumption of a system under steady state in calculating the temperature gradient over the glass wall (and remaining ice layer) via Fourier's law of thermal conduction might be no longer valid. Therefore, T_i might be overestimated for the few last minutes of the primary drying stage. Toward the end, the obtained T_i value exceeds the T_g' value of the formulation, i.e., −32.5 °C, while no macroscopic collapse was observed, which might confirm this hypothesis.[10]

3.5. Dried Product Mass Transfer Resistance. On the basis of the measurement of T_i, the dried product mass transfer resistance R_p is calculated using eq 4 and plotted as a function of the dried layer thickness l in Figure 8. The R_p profile has a shape similar to that of the T_i curve. R_p is plotted starting at a dried layer thickness of 0.0001 m because of ice sublimation during the initial pressure decrease in the drying chamber.[20] The steep increase in R_p at a dried layer thickness of approximately 0.0014 m is caused by the small increase in temperature after approximately 100 min of primary drying, as extensively described in the section 3.4. At this very end of primary drying, it was hypothesized that T_i was overestimated, in turn leading to an overestimation of R_p. Therefore, this last part of the R_p profile, indicated by the vertical line in Figure 8, was not included for the fitting of eq 9 to the R_p data.

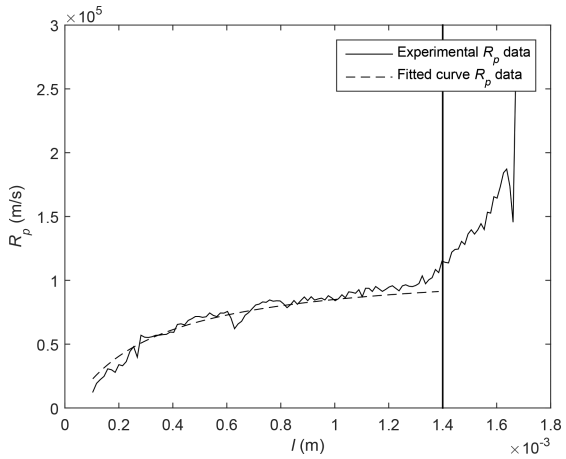

Figure 8. Dried product mass transfer resistance R_p (m/s) as a function of the dried layer thickness l (m). The R_p data on the right-hand side of the vertical line were not included in the fitting of the curve.

Via nonlinear regression, $R_{p,0} = -9.22 \times 10^3$ m/s (95% confidence interval (-2.10×10^4 m/s to 2.60×10^3 m/s), $A_{R_p} = 4.22 \times 10^8$ 1/s (2.79×10^8 1/s to 5.65×10^8 1/s), and $B_{R_p} = 3.48 \times 10^3$ 1/m (2.50×10^3 1/m to 4.46×10^3 1/m) were calculated. The 95% confidence interval for $R_{p,0}$ included zero, indicating that, at the start of primary drying ($l = 0$), R_p was minimal as no pores were present to limit the mass flow. Often, $R_{p,0}$ is assumed to be zero because of the theoretical absence of any product resistance when sublimation is initiated.[42] This condition was not imposed for the regression analysis, as this point was situated outside the experimental region, but the $R_{p,0}$ coefficient seems to confirm this theory.

With the increase in l, R_p increased toward a plateau value, as B_{R_p} is significantly different from zero. This behavior has been observed before for pure sucrose formulations and is attributed to the onset of microcollapse because of the very low T_g' value of the formulation (−32.5 °C).[7,30,42−44] The R_p profile starts to level when T_i approaches the T_g' value of the formulation, which might confirm the occurrence of microcollapse.

The results indicate that thermal imaging is a suitable technique to determine R_p as a function of l for spin-frozen vials. This is an important step regarding the development and optimization of the primary drying process conditions (i.e., the dynamic IR heater profile) for the continuous freeze-drying of a wide range of products.[22] In addition, the proposed procedure allows the development of a standardized method to evaluate the influence of different process and formulation parameters on R_p, which will lead to new insights in the development of the continuous freeze-drying technology.

4. CONCLUSION

Noninvasive thermal imaging was shown to be particularly suitable for inline real-time measurement of T_i for each vial during the primary drying step of the continuous freeze-drying concept, as opposed to the invasive temperature sensors applied during batch freeze-drying. As the sublimation front in spin-frozen vials moves in the direction of the glass wall, toward the thermal IR camera, T_i could be monitored during the entire primary drying step, after compensating for the temperature gradient over the glass wall and ice layer via Fourier's law of thermal conduction. On the basis of the monitoring of T_i, thermal imaging allowed the detection of the primary drying end point in spin-frozen vials, confirmed by NIR spectroscopy. In addition, this technique allowed the measurement of the dried product mass transfer resistance R_p as a function of the dried layer thickness l, essential for the optimization of the dynamic IR heater profile during the continuous freeze-drying of a specific product. The developed procedure can be applied as a standardized method to evaluate the effect of several process parameters on R_p, offering essential information for the further development of the continuous freeze-drying technology. Further, thermal imaging has the emerging potential for inline real-time control of T_i by a feedback loop steering the individual IR heaters, hence avoiding exceeding $T_{i,crit}$. Finally, this technology is also suitable for real-time temperature monitoring during the secondary drying stage in continuous freeze-drying.

■ ASSOCIATED CONTENT

Supporting Information

The Supporting Information is available free of charge on the ACS Publications website at DOI: 10.1021/acs.analchem.8b03788.

Description of the continuous freeze-drying concept and model-based design of the thermal camera setup (PDF)

■ AUTHOR INFORMATION

Corresponding Author

*T.D.B.: e-mail, Thomas.DeBeer@UGent.be; tel, +32(0)9 264 80 97; fax, +32(0)9 264 82 36.

DOI: 10.1021/acs.analchem.8b03788
Anal. Chem. 2018, 90, 13591−13599

ORCID

Pieter-Jan Van Bockstal: 0000-0002-0363-3618

Notes

The authors declare no competing financial interest.

■ ACKNOWLEDGMENTS

Financial support for this research from the Flanders Innovation & Entrepreneurship (VLAIO - Innovation mandate HBC.2017.0534 - Postdoctoral fellowship P.-J.V.B.) is gratefully acknowledged.

■ REFERENCES

(1) Jennings, T. *Lyophilization: Introduction and basic principles*; Informa Healthcare: New York, 2008.
(2) Koganti, V. R.; Shalaev, E. Y.; Berry, M. R.; Osterberg, T.; Youssef, M.; Hiebert, D. N.; Kanka, F. A.; Nolan, M.; Barrett, R.; Scalzo, G.; et al. *AAPS PharmSciTech* **2011**, *12*, 854−861.
(3) Kasper, J. C.; Friess, W. *Eur. J. Pharm. Biopharm.* **2011**, *78*, 248−263.
(4) Bogner, R.; Pikal, M. J. *Notes of Freeze Drying of Pharmaceuticals and Biologicals Conference, Garmisch-Partenkirchen* **2010**, 184−198.
(5) Mockus, L. N.; Paul, T. W.; Pease, N. A.; Harper, N. J.; Basu, P. K.; Oslos, E. A.; Sacha, G. A.; Kuu, W. Y.; Hardwick, L. M.; Karty, J. J.; et al. *Pharm. Dev. Technol.* **2011**, *16*, 549−576.
(6) Fissore, D.; Pisano, R.; Barresi, A. A. *J. Pharm. Sci.* **2011**, *100*, 4922−4933.
(7) Giordano, A.; Barresi, A. A.; Fissore, D. *J. Pharm. Sci.* **2011**, *100*, 311−324.
(8) Bosca, S.; Fissore, D.; Demichela, M. *Ind. Eng. Chem. Res.* **2015**, *54*, 12928−12936.
(9) Mortier, S.; Van Bockstal, P. J.; Corver, J.; Nopens, I.; Gernaey, K.; De Beer, T. *Eur. J. Pharm. Biopharm.* **2016**, *103*, 71−83.
(10) Van Bockstal, P.-J.; Mortier, S.; Corver, J.; Nopens, I.; Gernaey, K.; De Beer, T. *Eur. J. Pharm. Biopharm.* **2017**, *121*, 32−41.
(11) Nail, S.; Tchessalov, S.; Shalaev, E.; Ganguly, A.; Renzi, E.; Dimarco, F.; Wegiel, L.; Ferris, S.; Kessler, W.; Pikal, M.; et al. *AAPS PharmSciTech* **2017**, *18*, 2379−2393.
(12) Patel, S. M.; Doen, T.; Pikal, M. J. *AAPS PharmSciTech* **2010**, *11*, 73−84.
(13) Barresi, A. A.; Pisano, R.; Fissore, D.; Rasetto, V.; Velardi, S. A.; Vallan, A.; Parvis, M.; Galan, M. *Chem. Eng. Process.* **2009**, *48*, 408−423.
(14) Liapis, A. I.; Pikal, M. J.; Bruttini, R. *Drying Technol.* **1996**, *14*, 1265−1300.
(15) Tang, X.; Pikal, M. J. *Pharm. Res.* **2004**, *21*, 191−200.
(16) Chouvenc, P.; Vessot, S.; Andrieu, J.; Vacus, P. *Drying Technol.* **2004**, *22*, 1577−1601.
(17) Schneid, S.; Gieseler, H. *AAPS PharmSciTech* **2008**, *9*, 729−739.
(18) Velardi, S. A.; Rasetto, V.; Barresi, A. A. *Ind. Eng. Chem. Res.* **2008**, *47*, 8445−8457.
(19) De Meyer, L.; Van Bockstal, P. J.; Corver, J.; Vervaet, C.; Remon, J. P.; De Beer, T. *Int. J. Pharm.* **2015**, *496*, 75−85.
(20) Van Bockstal, P.-J.; De Meyer, L.; Corver, J.; Vervaet, C.; De Beer, T. *J. Pharm. Sci.* **2017**, *106*, 71−82.
(21) Corver, J. Method and system for freeze-drying injectable compositions, in particular pharmaceutical. Patent WO2013036107, 2013.
(22) Van Bockstal, P.-J.; Mortier, S.; De Meyer, L.; Corver, J.; Vervaet, C.; Nopens, I.; De Beer, T. *Eur. J. Pharm. Biopharm.* **2017**, *114*, 11−21.
(23) Emteborg, H.; Zeleny, R.; Charoud-Got, J.; Martos, G.; Lüddeke, J.; Schellin, H.; Teipel, K. *J. Pharm. Sci.* **2014**, *103*, 2088−2097.
(24) Lietta, E.; Colucci, D.; Distefano, G.; Fissore, D. *J. Pharm. Sci.* **2018**, DOI: 10.1016/j.xphs.2018.07.025.
(25) Liapis, A. I.; Bruttini, R. *Drying Technol.* **1995**, *13*, 43−72.
(26) Bird, R.; Stewart, W.; Lightfoot, E. *Transport phenomena*; Wiley: New York, 2006.
(27) Nellis, G. F.; Klein, S. A. *Heat Transfer*; Cambridge University Press: Cambridge, 2009.
(28) Van Bockstal, P.-J.; Corver, J.; Mortier, S. T. F.; De Meyer, L.; Nopens, I.; Gernaey, K. V.; De Beer, T. *Eur. J. Pharm. Biopharm.* **2018**, *127*, 159−170.
(29) Overcashier, D. E.; Patapoff, T. W.; Hsu, C. C. *J. Pharm. Sci.* **1999**, *88*, 688−695.
(30) Rambhatla, S.; Ramot, R.; Bhugra, C.; Pikal, M. J. *AAPS PharmSciTech* **2004**, *5*, 54−62.
(31) Kuu, W. Y.; Hardwick, L. M.; Akers, M. J. *Int. J. Pharm.* **2006**, *313*, 99−113.
(32) Pisano, R.; Fissore, D.; Barresi, A. a.; Brayard, P.; Chouvenc, P.; Woinet, B. *Pharm. Dev. Technol.* **2013**, *18*, 280−295.
(33) Vercruysse, J.; Toiviainen, M.; Fonteyne, M.; Helkimo, N.; Ketolainen, J.; Juuti, M.; Delaet, U.; Van Assche, I.; Remon, J. P.; Vervaet, C.; et al. *Eur. J. Pharm. Biopharm.* **2014**, *86*, 383−392.
(34) Eriksson, L.; Johansson, E.; Kettaneh-Wold, N.; Trygg, J.; Wikström, C.; Wold, S. *Multi- and megavariate data analysis part 1: Basic principles and applications*; Umetrics: Umeå, 2006.
(35) Pieters, S.; Vander Heyden, Y.; Roger, J. M.; D'Hondt, M.; Hansen, L.; Palagos, B.; De Spiegeleer, B.; Remon, J. P.; Vervaet, C.; De Beer, T. *Eur. J. Pharm. Biopharm.* **2013**, *85*, 263−271.
(36) Lammens, J.; Mortier, S.; De Meyer, L.; Vanbillemont, B.; Van Bockstal, P.-J.; Van Herck, S.; Corver, J.; Nopens, I.; Vanhoorne, V.; De Geest, B.; et al. *Int. J. Pharm.* **2018**, *539*, 1−10.
(37) Kauppinen, A.; Toiviainen, M.; Korhonen, O.; Aaltonen, J.; Paaso, J.; Juuti, M.; Ketolainen, J. *Anal. Chem.* **2013**, *85*, 2377−2384.
(38) Brouckaert, D.; De Meyer, L.; Vanbillemont, B.; Van Bockstal, P. J.; Lammens, J.; Mortier, S.; Corver, J.; Vervaet, C.; Nopens, I.; De Beer, T. *Anal. Chem.* **2018**, *90*, 4354−4362.
(39) De Beer, T. R. M.; Wiggenhorn, M.; Veillon, R.; Debacq, C.; Mayeresse, Y.; Moreau, B.; Burggraeve, A.; Quinten, T.; Friess, W.; Winter, G.; et al. *Anal. Chem.* **2009**, *81*, 7639−7649.
(40) De Beer, T. R. M.; Vercruysse, P.; Burggraeve, A.; Quinten, T.; Ouyang, J.; Zhang, X.; Vervaet, C.; Remon, J. P.; Baeyens, W. R. G. *J. Pharm. Sci.* **2009**, *98*, 3430−3446.
(41) Pieters, S.; De Beer, T.; Kasper, J. C.; Boulpaep, D.; Waszkiewicz, O.; Goodarzi, M.; Tistaert, C.; Friess, W.; Remon, J. P.; Vervaet, C.; et al. *Anal. Chem.* **2012**, *84*, 947−955.
(42) Konstantinidis, A.; Kuu, W.; Otten, L.; Nail, S.; Sever, R. *J. Pharm. Sci.* **2011**, *100*, 3453−3470.
(43) Kuu, W.; O'Brien, K.; Hardwick, L.; Paul, T. *Pharm. Dev. Technol.* **2011**, *16*, 343−357.
(44) Chen, R.; Slater, N. K. H.; Gatlin, L. A.; Kramer, T.; Shalaev, E. Y. *Pharm. Dev. Technol.* **2008**, *13*, 367−374.

DOI: 10.1021/acs.analchem.8b03788
Anal. Chem. 2018, 90, 13591−13599